Cryo-electron tomography of Birbeck granules reveals the molecular mechanism of langerin lattice formation

Authors: Toshiyuki Oda[1*], Haruaki Yanagisawa[2], Hideyuki Shinmori [3], Youichi Ogawa[4], and Tatsuyoshi Kawamura[4]

Affiliations: [1] Department of Anatomy and Structural Biology, Graduate School of Medicine, University of Yamanashi, 1110 Shimokato, Chuo, Yamanashi, 409-3898, Japan. [2] Department of Cell Biology and Anatomy, Graduate School of Medicine, the University of Tokyo, 7-3-1 Hongo, Bunkyo-ku, Tokyo, 113-0033, Japan.

[3] Faculty of Life and Environmental Science, University of Yamanashi, 4-4-37 Takeda, Kofu, Yamanashi, 400-8510, Japan

[4] Department of Dermatology, Faculty of Medicine, University of Yamanashi, 1110 Shimokato, Chuo, Yamanashi, 409-3898, Japan.

*Correspondence to: toda@yamanashi.ac.jp

Abstract

Langerhans cells are specialized antigen-presenting cells localized within the epidermis and mucosal epithelium. Upon contact with Langerhans cells, pathogens are captured by the C-type lectin langerin and internalized into a structurally unique vesicle known as a Birbeck granule. Although the immunological role of Langerhans cells and Birbeck granules have been extensively studied, the mechanism by which the characteristic zippered membrane structure of Birbeck granules is formed remains elusive. In this study, we observed isolated Birbeck granules using cryo-electron tomography and reconstructed the 3D structure of the repeating unit of the honeycomb lattice of langerin at 6.4 Å resolution. We found that the interaction between the two langerin trimers was mediated by docking the flexible loop at residues 258-263 into the secondary carbohydrate-binding cleft. Mutations within the loop inhibited Birbeck granule formation and the internalization of HIV pseudovirus. These findings suggest a molecular mechanism for membrane zippering during Birbeck granule biogenesis and provide insight into the role of langerin in the defense against viral infection.

35 **Introduction**

36 The epidermis and mucosa provide the first line of defense against pathogens. In these tissues,
37 specialized antigen-presenting cells called Langerhans cells capture pathogens by
38 recognizing their surface mannose-containing oligosaccharides via the C-type lectin
39 langerin (Valladeau et al., 2003; Doebel et al., 2017). Pathogens internalized via langerin are
40 enclosed in a specialized organelle called a Birbeck granule, which has a central striated
41 lamella between closely apposed membranes (Birbeck et al., 1961; Valladeau et al., 2000;
42 McDermott et al., 2004; Valladeau et al., 1999). Once pathogens are captured, Langerhans
43 cells undergo maturation and migrate to peripheral lymph nodes, where they present
44 processed antigens to T cells (Merad et al., 2008; de_Jong MA, 2010; Rhodes et al., 2021).
45 Langerin is a type II transmembrane protein that is composed of a cytoplasmic tail, coiled-
46 coil neck region, and carbohydrate recognition domain (CRD) (Stambach and Taylor, 2003;
47 Valladeau et al., 1999; Valladeau et al., 2000) (Figure 1A). Through the coiled-coil neck
48 region, langerin forms a trimer, which is functionally important for oligosaccharide binding
49 (Stambach and Taylor, 2003; Weis and Drickamer, 1996; Weis and Drickamer, 1994). The
50 calcium-dependent carbohydrate-binding capacity of langerin CRD is essential for the
51 formation of Birbeck granules because the removal of calcium ions causes them to unzip and

52 disintegrate (Stambach and Taylor, 2003; Bartosik, 1992). It has been proposed that the "face-
53 to-face" interaction between the langerin trimers via CRDs confers the characteristic zippered
54 membranes with a central striation of Birbeck granules (Thepaut et al., 2009) (Figure 1B and
55 1C). However, the precise molecular mechanism of Birbeck granule formation is unknown
56 because of the lack of a high-resolution structure.

57 Langerin's high affinity for mannose and oligo-mannose allows Langerhans cells to capture
58 a wide range of pathogens, including *Saccharomyces cerevisiae, Candida albicans,*
59 *Mycobacterium leprae,* herpes simplex virus, and human immunodeficiency virus-1 (HIV-1)
60 (Tateno et al., 2010; Hunger et al., 2004; de Jong et al., 2010; de Witte et al., 2007; Turville et al.,
61 2002). Although Langerhans cells in the mucosa are the initial target of HIV-1 in sexually
62 transmitted infections, the efficiency of Langerhans cell infection is low, requiring high viral
63 loads of HIV-1 to infect cells (Kawamura et al., 2001; Kawamura et al., 2000; Ogawa et al., 2013).
64 The resistance of Langerhans cells to HIV-1 infection is mediated by the efficient internalization
65 of HIV-1 into Birbeck granules and subsequent autophagic degradation (de Witte et al., 2007;
66 Ribeiro et al., 2016). Therefore, elucidating the mechanism by which HIV-1 is internalized into
67 Birbeck granules is essential to understanding the role of Langerhans cells as a barrier to HIV-1
68 infection.

69 In the present study, we reconstructed the 3D structure of isolated Birbeck granules using cryo-
70 electron tomography and identified a flexible loop region that is crucial for Birbeck granule
71 formation and virus internalization.
72
73 **Results**
74 **Cryo-electron microscopy of isolated Birbeck granules**
75 Exogenous expression of langerin in mammalian cell lines readily reproduces the formation
76 of Birbeck granules (McDermott et al., 2004). We found that the addition of yeast mannan to
77 langerin-expressing cells enhances the formation of large Birbeck granules (Figure 1C). To
78 purify these Birbeck granules, we expressed SNAP-tagged human langerin in 293T cells,
79 biotinylated the tag by incubation with benzylguanine-biotin, and immunoprecipitated the
80 Birbeck granules using streptavidin agarose (Figure 1D and S1A). Under cryo-electron
81 microscopy, the isolated Birbeck granules were observed to be thin lamellar vesicles of
82 assorted sizes, similar to those reported previously (Figure 1E, 1F, and S1B) (Sagebiel and
83 Reed, 1968; Lenormand et al., 2013). Unlike regular 2D crystals of proteins, Birbeck
84 granules appear wavy, suggesting structural heterogeneity. The 2D classification of the
85 segmented images extracted from the micrographs showed nearly three-fold symmetrical

86 arrangements of pores with a diameter of approximately 10 nm; however, no clear crystalline
87 lattice was observed (Figure 1G). Although most Birbeck granules were oriented in
88 approximately the same direction with respect to the beam axis, some granules were twisted,
89 providing different views that were sufficient for 3D reconstruction (Figure S1C).
90

91 **Subtomogram averaging of the repeating unit of Birbeck granules**

92 We conducted cryo-electron tomography of the isolated Birbeck granules and reconstructed
93 the repeating units by averaging the subtomograms (Figure 2 and S2A). The initial density
94 map (Figure 2A) shows a langerin trimer (blue) with three inverted trimers (red) attached to
95 the CRDs. However, because of the flexibility between each langerin trimer, the resolution
96 was limited to ~24 Å. To improve the resolution, we generated a mask enclosing the central
97 langerin trimer and three attached CRDs and performed focused refinement and 3D
98 classification (Figure 2B). The resolution was improved to 6.4 Å (Figure S2B), which clearly
99 visualized the alpha helices and enabled us to generate a model based on the previously
100 reported crystal structure of the langerin trimer (Feinberg et al., 2010). We then performed a
101 two-body refinement to visualize the spatial relationship between the two opposing langerin
102 trimers (Nakane et al., 2018). Based on this refinement (Figure 2C), we built a honeycomb

103 lattice model (Figure 2D and Movie S1), which agrees with the striation of the Birbeck
104 granules observed by ultra-thin section electron microscopy and the ~10 nm pores visualized
105 in the 2D classification images (Figure 1C and 1G) (Birbeck et al., 1961). However, in reality,
106 the honeycomb lattice is non-uniform because of the structural heterogeneity.
107

108 **Interaction between the two langerin trimers via flexible loops**

109 An in-depth analysis of the interaction region between the two CRDs (Figure 3) revealed that
110 the interaction is mediated by a loop at residues 258-263, which is highly flexible in the
111 crystal structure (Feinberg et al., 2010). The interaction between the two CRDs appears to be
112 maintained by docking the loops of two langerin molecules into each other's lateral cleft,
113 which constitutes the secondary carbohydrate-binding site (Figure 3A, pink circles)
114 (Chatwell et al., 2008). The interaction between the two CRDs is flexible because the first
115 eigenvector of the multi-body analysis represents an approximately 30° tilting motion with
116 the loop as the fulcrum (Figure 3B, and Movie S2). Interestingly, loop 258-263 of the inverted
117 molecule appears to participate in the secondary carbohydrate-binding site of the upright
118 molecule (Figure 3A). A previous study found that the secondary calcium-independent
119 binding site has a lower affinity for carbohydrate ligands than the primary calcium-dependent

120 binding site (Chatwell et al., 2008). The docked loop 258-263 may provide additional
121 interactions with the hydroxyl group of mannose via Glu261 and Asp263, thus increasing the
122 affinity of the secondary binding site when two langerin trimers form a complex. Furthermore,
123 the Trp264Arg mutation is associated with a lack of Birbeck granules (Verdijk et al., 2005;
124 Figdor et al., 2002). Trp264 may also be involved in docking the loop into the cleft; however,
125 it is more likely that disruption of the hydrophobic core of the CRD is responsible for this
126 defect in Birbeck granule formation (Chatwell et al., 2008).
127

128 **Loop 258-263 is essential for Birbeck granule formation**

129 To investigate the importance of loop 258-263 in the biogenesis of Birbeck granules, we
130 mutated three residues in the loop: Met260Ala, Glu261Arg, and Asp263Lys, and generated
131 three mutated langerin constructs, each carrying one (MRGD), two (MRGK), or three
132 mutations (ARGK). We expressed these three langerin mutants in 293T cells and induced
133 Birbeck granule formation by adding yeast mannan (Figure 4A). Under ultra-thin section
134 microscopy, wild-type langerin produced Birbeck granules a few micrometers in length in
135 the presence of mannan (Figure 4A, MEGD WT). As the number of mutations increased, the
136 length of Birbeck granules decreased. With two point mutations (MRGK), some cross-

137 sections became spherical rather than rod-shaped, suggesting that the Birbeck granules failed
138 to extend. With three mutations (ARGK), clusters of Birbeck granules were not observed,
139 with isolated individual granules observed instead. The length of individual Birbeck granules
140 and the total length of granules per area were measured to confirm the above observations
141 (Figure 4B and 4C). In contrast, the number of the Birbeck granules showed less significant
142 differences because numerous short fragments were present in the mutant specimen (Figure
143 4D). These results demonstrate the importance of loop 258-263 in the biogenesis of Birbeck
144 granules.
145
146 **Loop 258-263 is crucial for the internalization of HIV pseudovirus**
147 To investigate the impact of the mutations in loop 258-263 on virus internalization by Birbeck
148 granules, we added lentiviruses pseudo-typed with the HIV-1 env protein to langerin-
149 expressing 293T cells. After 30 min of incubation, we retrieved viruses attached to the surface
150 langerin by washing with EDTA buffer, removed non-specifically attached viruses by
151 trypsinization, and isolated the Birbeck granules using streptavidin-agarose (Figure 5). A
152 langerin mutant that lost its calcium-binding capacity (Stambach and Taylor, 2003) was used
153 as the negative control (Figure 5, lectin (-)). The HIV pseudoviruses attached to both wild-

154 type and ARGK mutant langerin and the attachment was abolished by the addition of mannan
155 (Figure 5A). This indicated that the mutation of the loop did not disrupt the binding of the
156 glycosylated envelope proteins to the primary carbohydrate-binding sites. In contrast, the
157 internalization of the pseudovirus was significantly inhibited by the ARGK mutation (Figure
158 5B and 5C). These results suggest that disruption of Birbeck granule formation by the
159 mutation of loop 258-263 inhibited the internalization of HIV pseudovirus.
160

161 **Discussion**

162 **Virus internalization mechanism of Birbeck granules**

163 In the present study, we reconstructed the 3D structure of isolated Birbeck granules and found
164 that docking of the flexible loop 258-263 into the secondary carbohydrate-binding cleft is
165 essential for assembly of the langerin lattice. In agreement with this observation, we showed
166 that mutations introduced into the loop inhibited Birbeck granule formation and
167 internalization of HIV pseudovirus. Based on the structure of the glycosylated HIV env
168 protein (Stewart-Jones et al., 2016; Pan et al., 2020), we propose a model of HIV
169 internalization by langerin (Figure 6A and 6B). A previous study proposed that N-linked
170 high-mannose oligosaccharides bind to langerin at both primary and secondary carbohydrate-

171 binding sites (Chatwell et al., 2008). Our model requires bending of the coiled-coil necks of
172 the two langerin trimers to form a complex with HIV-1 env via the high-mannose
173 oligosaccharide (Figure 6B). Although the triple coiled-coil structure of the neck domain
174 does not seem to bend strongly, the coiled-coil prediction profile suggests that the N-terminal
175 part of the neck does not necessarily form a rigid triple coiled coil (Lupas et al., 1991) (Figure
176 S1D). Thus, we speculate that the neck region of the langerin trimer is flexible and swings
177 on the cell surface, allowing loop 258-263 of one trimer to dock into the cleft of an adjacent
178 trimer. Once the triad structure, consisting of two langerin trimers and one env protein, is
179 formed, the elasticity of the neck region can deform the cell membrane and initiate
180 invagination. The formation of clathrin pits may also be involved in membrane invagination,
181 because the cytoplasmic ends of Birbeck granules are coated with clathrin (Mc et al., 2002).
182 Additionally, it is possible that other intracellular mechanisms such as the actin cytoskeleton,
183 are involved in this membrane deformation process because annexin A2 is required for the
184 proper formation of Birbeck granules (Thornton et al., 2020).
185

186 **Significance of langerin-specific secondary carbohydrate-binding cleft**

187 It is noteworthy that the docking of loop 258-263 into the secondary calcium-independent

188 carbohydrate-binding cleft, which is not found in other C-type lectins (Chatwell et al., 2008),
189 mediates the assembly of the langerin lattice. In DC-SIGN, which is another C-type lectin
190 expressed in dendritic cells, and is closely related to langerin, the region corresponding to the
191 secondary carbohydrate-binding site of langerin forms a shallow pocket, that is occupied by
192 two calcium ions (Figure 7A) (Guo et al., 2004; Geijtenbeek et al., 2000; Geijtenbeek et al.,
193 2000). This structural difference between langerin and DC-SIGN may account for the
194 inability of DC-SIGN to form Birbeck granules despite its high sequence similarity to
195 langerin (Cambi et al., 2009). Another characteristic of the secondary carbohydrate-binding
196 site of langerin is its weak affinity for mannose and maltose (Chatwell et al., 2008). This may
197 reflect that the sugar-binding surface of langerin CRD is less negatively charged than that of
198 DC-SIGN CRD (Figure 7A) (Chatwell et al., 2008). Moreover, the interaction between the
199 secondary binding site and mannose/maltose is mainly mediated by backbone amide and
200 carbonyl groups (Chatwell et al., 2008). It is possible that the side chains of Glu261 and
201 Asp263 of loop 258-263 docked into the cleft of an adjacent langerin CRD provide the
202 negative charge required for stabilizing oligo-mannose bound to the secondary binding site
203 (Figure 7A and B). In agreement with this hypothesis, in the present study the Asp263Lys
204 mutation caused a significant defect in Birbeck granule formation. The secondary

205 carbohydrate-binding site may only be fully functional when two langerin trimers are bound
206 to each other (Figure 6 and 7B). The effect of the Met260Ala mutation on Birbeck granule
207 formation was unexpected, because the mutation was supposed to be silent in terms of side
208 chain charge. The observed structural variation of the langerin trimer complex suggests that
209 the side chain of Met260 acts as a hook to stabilize the interface between the two intersecting
210 loops.
211 Our model of Birbeck granule formation suggests that oligosaccharide ligands are captured
212 by the lateral surface of langerin (Figure 6). In contrast, DC-SIGN binds to dengue virus on
213 its upper surface (Pokidysheva et al., 2006). The difference in the ligand-binding manner
214 between langerin and DC-SIGN may contribute to their different carbohydrate recognition
215 preferences (Valverde et al., 2020; Takahara et al., 2004). Further studies are needed to
216 investigate the physiological significance of the unique carbohydrate-binding mechanism of
217 langerin and the honeycomb lattice structure of Birbeck granules.
218
219

220 **Methods**

221 ***Isolation of Birbeck granules***

222 The cDNA of human langerin was obtained from the Mammalian Gene Collection library
223 (Dnaform Inc., Yokohama, Japan) and was subcloned into pcDNA3.1-IRES-GFP (Schaefer
224 et al., 2008). A codon-optimized sequence coding SNAP-3×HA-HRV3C cleavage site
225 (obtained from ThermoFisher Scientific, Waltham, MA) was inserted immediately before the
226 start codon of the langerin sequence (Cole, 2013). O^6-benzylguanine-biotin was obtained by
227 reacting 16 mM O^6-benzylguanine-amine (Accela ChemBio, Shanghai, China) with 50 mM
228 biotin-AC_5-Osu (Dojindo, Kumamoto, Japan) and 30 mM triethylamine in
229 dimethylformamide for 24 hours at 30℃. Lenti-X 293T cells (TakaraBio, Tokyo, Japan) were
230 transfected with the langerin-expression plasmid by electroporation using ECM630
231 electroporator (BTX, Holliston, MA) and seeded onto the polyethylenimine-coated dish (PEI,
232 obtained from Fujifilm Wako Chemicals, Osaka, Japan). After 48-hour culturing in
233 DMEM+10% fetal bovine serum (FBS), the culture medium was replaced with serum-free
234 DMEM containing 10 μM O^6-benzylguanine-biotin and 10 μg/ml yeast mannan (Nacalai
235 tesque, Kyoto, Japan) and the cells were incubated for 30 min at 37 ℃. The cells were then
236 collected by scraping and washed five times with isotonic HMC buffer (Hepes 30 mM, pH

237 7.2, 150 mM NaCl, 2 mM $MgCl_2$, 2 mM $CaCl_2$, protease inhibitor cocktail (Nacalai tesque)).
238 The washed cells were homogenized with a Dounce glass homogenizer and were further
239 disrupted by sonication for 8 seconds using a Q125 sonicator (Qsonica, Newtown, CT). The
240 cell homogenate was loaded on top of a discontinuous Opti-prep density gradient (10-20-
241 40% layers, ThermoFisher Scientific) and ultracentrifuged for 1 hour at 100,000×g. The
242 fraction at the interface of 20/40% layers was collected and diluted 10-fold with HMC buffer
243 and was again disrupted by sonication for 2 min (120 cycles of 1-sec pulse and 3-sec wait)
244 at 4℃. Large debris was removed by filtration through a 20 μm-pore polyethylene mesh (GL
245 Science, Tokyo, Japan) and the cell lysate was incubated with a 30 μl slurry of streptavidin
246 agarose (Solulink, San Diego, CA) overnight at 4℃. The streptavidin agarose beads were
247 washed five times with HMC buffer and the bound Birbeck granules were eluted by overnight
248 digestion using home-made E. coli overexpressed His×6-HRV3C protease in HMC buffer at
249 4℃. After digestion and elution, HRV3C protease was removed by incubating the elute with
250 Ni-NTA resin (Qiagen, Düsseldorf, Germany). About 50 μl of elute containing released
251 Birbeck granules (approximately 0.05 mg/ml) were obtained from twelve 100-mm dishes of
252 cell culture.
253

254 ***Cryo-electron microscopy of isolated Birbeck granules***

255 5 µl of the purified Birbeck granules was applied onto freshly glow-discharged holey carbon
256 grids, Quantifoil R1.2/1.3 Cu/Rh 200 mesh (Quantifoil Micro Tools GmbH, Großlöbichau,
257 Germany), blotted from the backside to concentrate the granules by filtration through the
258 holes, and 4 µl of HMC buffer containing cytochrome *c*-stabilized 15-nm colloidal gold (BBI
259 Solutions) was applied for attachment of fiducial markers (Oda et al., 2015). Grids were
260 blotted from the backside for 10 seconds at 4℃ under 99% humidity and plunge frozen in
261 liquid ethane using Vitrobot Mark IV (Thermo Fisher Scientific). We removed one of the
262 blotting arms for one-side blotting because Birbeck granules would be absorbed onto the
263 filter paper. Images were recorded using a Titan Krios G3i microscope at the University of
264 Tokyo (Thermo Fisher Scientific) at 300 keV, a Gatan Quantum-LS Energy Filter (Gatan,
265 Pleasanton, CA) with a slit width of 20 eV, and a Gatan K3 Summit direct electron detector
266 in the electron counting mode. The nominal magnification was set to 33,000× with a physical
267 pixel size of 2.67 Å/pixel. Movies were acquired using the SerialEM software (Mastronarde,
268 2005), and the target defocus was set to 3-6 µm. The angular range of the tilt series was from
269 -60° to 60° with 3.0° increments. Each movie was recorded for 0.74 sec with a total dose of
270 1.24 electrons/$Å^2$ and subdivided into 20 frames. The total dose for one tilt series acquisition

271 is thus 50 electrons/Å^2.

272

273 ***Data processing***

274 Movies were subjected to beam-induced motion correction using MotionCor2 (Zheng et al.,
275 2017), and tilt series images were aligned, CTF corrected, and back-projected to reconstruct
276 3D tomograms using the IMOD software package (Kremer et al., 1996). For the subsequent
277 analysis using Relion-4.0 (Kimanius et al., 2021), the tomogram positioning step was skipped
278 to keep the angle offset and the Z-shift zero. Tomograms were 4×binned to reduce loads of
279 the calculation. The areas of the Birbeck granules were manually selected using the 3dmod
280 model tool (Kremer et al., 1996), and the center coordinates for the subtomograms were
281 determined by placing points at 8-pixel (~8.5 nm) intervals within the selected area using a
282 custom-made Ruby script (Metlagel et al., 2007). For twisting Birbeck granules (Figure S1C),
283 center points were picked manually by selecting the mid-portion of the lamella. Volumes with
284 32×32×32 pixel-dimensions were extracted from 8×binned tomograms and were averaged
285 using the PEET software suite (Nicastro et al., 2006). A randomly selected subtomogram was
286 used for the initial reference. Alignments were repeated five times for 8×binned and twice
287 for 4×binned tomograms with 64×64×64 pixel-dimensions. The coordinates and the rotation

288 angles of the aligned subtomograms were exported to Relion-4.0. Initial
289 pseudosubtomograms were generated with the box size of 128 pixels, the cropped box size
290 of 64 pixels, and the binning factor of 4. The subtomograms were 3D refined using a spherical
291 mask of 320-Å diameter. After 3D classification, 2×binned pseudosubtomograms were
292 generated with the box size of 256 pixels and the cropped box size of 128 pixels based on the
293 refined coordinates and angles and were 3D refined using the same spherical mask. Finally,
294 un-binned pseudosubtomograms were generated with a box size of 256 pixels and a cropped
295 box size of 128 pixels. 3D refinement was done using a tighter mask enclosing the central
296 upright langerin molecule and three bound CRDs, and low-resolution subtomograms were
297 removed by 3D classification. The alignment was further refined using CTF refinement and
298 frame alignment. We initially refined the surrounding inverted langerin molecule by 3D
299 refinement masking out the central upright molecule, but the refinement was biased toward
300 the center. To improve the map quality of the inverted molecule, we applied 3D multi-body
301 refinement (Nakane et al., 2018), which successfully compensated for the flexibility between
302 the upright and the inverted molecules. For model building, the crystal structure of langerin
303 trimer (Feinberg et al., 2010) (PDB ID: 3KQG) was fitted into the map using UCSF Chimera
304 (Pettersen et al., 2004). Then, the fitted model was further refined using PHENIX real-space

305 refinement tool, and the refined model was validated using the comprehensive validation tool
306 (Adams et al., 2010). The Coulombic surfaces rendering was conducted using UCSF
307 Chimera and other model presentations, surface rendering, and morph movie generation were
308 conducted using ChimeraX (Goddard et al., 2018). The data processing and the statistics of
309 the model validation are summarized in Figure S2A and Table S1.
310

311 ***Ultrathin section electron microscopy of Birbeck granules***

312 Pellets of 293T cells with mannan-induced Birbeck granules were fixed with 4%
313 paraformaldehyde for 1 hour at 4℃ and stained with 1% osmium tetroxide and subsequently
314 with 1% uranium acetate. After dehydration in ethanol and acetone, the samples were
315 embedded in Quetol 812 resin (Nissin EM, Tokyo, Japan). 60-nm ultrathin sections were
316 cut using a ULTRACUT microtome (Reichert Leica) and mounted onto Formvar-coated
317 copper grid. Images were recorded using a JEM-2100F microscope (JEOL, Tokyo, Japan) at
318 University of Yamanashi operated at 200 keV equipped with an F216 CMOS camera (TVIPS
319 GmbH, Gauting, Germany). Length of Birbeck granules were measured using Fiji software
320 (Schindelin et al., 2012), and plots were generated using PlotsOfData web tool (Postma and
321 Goedhart, 2019). For total length of Birbeck granules per 100 μm^2, cross sections of cells

322 with nuclei of > 5 μm in diameter were selected, and the sum of the lengths of Birbeck
323 granules within the cells were measured. The areas of the cross sections were also measured
324 using Fiji software. 100 μm^2 corresponds to the approximate mean of the cross-sectional area
325 of one cell.
326
327 ***Lentivirus preparation***
328 Lentiviruses pseudotyped with HIV-1 env were prepared by transfecting the Lenti-X 293T
329 cells with pCMV-dR8.3 Δvpr (Addgene plasmid #8455), pLOX-CW-tdTomato, and pCEP4-
330 AD8gp160 (Adgene plasmid #123260) (Stewart et al., 2003; Heredia et al., 2019). The vector
331 pLOX-CW-tdTomato was generated by replacing the GFP sequence of pLOX-CWgfp
332 (Addgene plasmid #12241) (Salmon et al., 2000) with the tdTomato sequence derived from
333 pCDH-EF1-Luc2-P2A-tdTomato, a gift from Kazuhiro Oka (Addgene plasmid # 72486). The
334 transfections were carried out using the PEI-method with the ratio at PEI: dR8.3: tdTomato:
335 gp160 = 4:1:1:1. 16 hours post-transfection, the cells were washed three times with PBS and
336 incubated in a fresh medium for another 32 hours. The virus-containing medium was
337 collected and removed cell debris by a 1,000×g centrifuge and a 0.45 μm filtration (Millipore).
338 The obtained supernatants were immediately used for subsequent assays.

339

340 ***Virus attachment and internalization assay***

341 293T cells were transfected with wild type langerin, the ARGK mutant, and, as a negative
342 control, a lectin (-) mutant lacking calcium-binding ability. The lectin (-) langerin mutant was
343 generated by introducing three point-mutations at the calcium-binding site: Glu285Lys;
344 Asn287Lys; and Glu293Lys (Chatwell et al., 2008). We conducted surface labeling of
345 langerin-expressing cells and confirmed that these mutations did not alter the surface
346 expression of langerin (Figure S3A). 48 hours post-transfection, the cells were pre-treated
347 with or without 10 μg/ml yeast mannan for 5 min at 37℃. The cells were then incubated in
348 the pseudovirus-containing supernatants plus 10 μM O^6-benzylguanine-biotin and 10 μg/ml
349 DEAE-dextran (Sigma Aldrich, St. Louis, MO) with or without 10 μg/ml yeast mannan for
350 30 min at 37℃. After the incubation, supernatant containing unbound viruses were collected.
351 The cells were then washed with TBS-Ca buffer (20 mM Tris-HCl pH 7.4, 150 mM NaCl, 5
352 mM $CaCl_2$) three times, and the viruses attached to langerin at the cell surface was retrieved
353 by washing with TBS-EDTA buffer (20 mM Tris-HCl pH 7.4, 150 mM NaCl, 10 mM EDTA).
354 The collected supernatant of the medium and the TBS-EDTA buffer were centrifuged at
355 1,000×g for 5 min to remove cell debris, and the viruses were sedimented by ultra-

356 centrifugation at 100,000×g for 3 hours. After the TBS-EDTA washing, non-specifically
357 bound viruses were removed by trypsinization using 0.25 % (w/v) trypsin and 1mM EDTA
358 for 5 min at 37℃ as previously described (Burkard et al., 2014). Detached cells were washed
359 twice with DMEM+10 % FBS, and five times with TBS-Ca. Internalized viruses within
360 Birbeck granules were isolated from the washed cells by streptavidin-agarose precipitation
361 as described above. Viruses, langerin, and tubulin were detected by immunoblotting using
362 HIV-1 gag p24 antibody (1:1000 dilution, MAB7360, mouse monoclonal, R&D systems,
363 Minneapolis, MN), human CD207 antibody (1:1000 dilution, 11841-1-AP, rabbit polyclonal,
364 Proteintech Group Inc., Rosemont, IL), and tubulin antibody (1:3000 dilution, B-512, mouse
365 monoclonal, Sigma-Aldrich), respectively. ELSA was carried out using HIV Type 1 p24
366 Antigen ELISA kit (ZeptoMatrix, Buffalo, NY). The p24 antibody detected unprocessed
367 ($Pr55^{gag}$) and fully processed (p24) capsid proteins (Gonelli et al., 2019). Band intensities
368 were measured using ImageJ (Schneider et al., 2012). Surface labeling was carried out by
369 treating the cells with 0.5mM biotin-sulfo-osu (Dojindo, Osaka, Japan) for 30 min at 37℃.
370 Cells were washed three times with TBS and collected by scraping. Surface-expressed
371 proteins were extracted by incubating the cells in TBS plus 1% Triton X-100 for 1 hour at
372 4℃, and immunoprecipitated using streptavidin agarose. ELISA using p24 antibody showed

373 that >99% of the viruses remained in the supernatant (Figure S3B).

374

375 ***Isolation of langerin-expressing stable cell lines***

376 We isolated a cell line stably expressing langerin by selecting HEK293 cells using G418

377 (Sigma Aldrich). However, the expression levels of the isolated cell line was 10~20% of that

378 of the transiently expressing cells (Figure S3C). These cells can form Birbeck granules in the

379 presence of yeast mannan, but with lower efficiency (Figure S3D and E). Therefore, we chose

380 to use the transient expression system in the main experiments.

381

382

383 **Author contributions**

384 T.O. conceived the project and designed the experiments. T.O., H.Y., and H.S. performed the
385 experiments. T.O., and H.Y. analyzed the data. T.O., H.Y., Y.O., and T.K. wrote the
386 manuscript.

387

388 **Data availability**

389 The map and the model will be available on the EMDB upon publication under the following
390 accession numbers: EMD-32906, and PDB 7WZ8.

391

392 **Acknowledgements**

393 We thank Mrs. Natsuko Maruyama (University of Yamanashi) for technical assistance. This
394 research is partially supported by Platform Project for Supporting Drug Discovery and Life
395 Science Research (Basis for Supporting Innovative Drug Discovery and Life Science
396 Research (BINDS)) from Japan Agency for Medical Research and Development (AMED)
397 under Grant Number JP19am0101115. This research was conducted using the Fujitsu
398 PRIMERGY CX400M1/CX2550M5 (Oakbridge-CX) and the SGI Rackable C2112-
399 4GP3/C1102-GP8 (Reedbush-H/L) in the Information Technology Center, The University of

Tokyo. This work was supported by the Takeda Science Foundation (to T.O.), the Daiichi Sankyo Foundation of Life Science (to T.O.), the Japan Society for the Promotion of Science (KAKENHI Grant number JP21H02654 to T.O.), and the Naito Foundation (to T.O.). Molecular graphics and analyses performed with UCSF ChimeraX, developed by the Resource for Biocomputing, Visualization, and Informatics at the University of California, San Francisco, with support from National Institutes of Health R01-GM129325 and the Office of Cyber Infrastructure and Computational Biology, National Institute of Allergy and Infectious Diseases.

410 **References**

411

412 Birbeck, M.S., Breathnach, A.S., and Everall, J.D. 1961. An electron microscope study of
413 basal melanocytes and high-level clear cells (Langerhans cells) in vitiligo. *J. Invest.*
414 *Dermatol.* **37**, 51-63.

415 Sagebiel, R.W., and Reed, T.H. 1968. Serial reconstruction of the characteristic granule of
416 the Langerhans cell. *J. Cell. Biol.* **36**, 595-602.

417 Lupas, A., Van, Dyke M., and Stock, J. 1991. Predicting coiled coils from protein
418 sequences. *Science.* **252**, 1162-1164.

419 Bartosik, J. 1992. Cytomembrane-derived Birbeck granules transport horseradish
420 peroxidase to the endosomal compartment in the human Langerhans cells. *J. Invest.*
421 *Dermatol.* **99**, 53-58.

422 Weis, W.I., and Drickamer, K. 1994. Trimeric structure of a C-type mannose-binding
423 protein. *Structure.* **2**, 1227-1240.

424 Kremer, J.R., Mastronarde, D.N., and McIntosh, J.R. 1996. Computer visualization of
425 three-dimensional image data using IMOD. *J. Struct. Biol.* **116**, 71-76.

426 Weis, W.I., and Drickamer, K. 1996. Structural basis of lectin-carbohydrate recognition.
427 *Annu. Rev. Biochem.* **65**, 441-473.

428 Valladeau, J., Duvert-Frances, V., Pin, J.J., Dezutter-Dambuyant, C., Vincent, C.,
429 Massacrier, C., Vincent, J., Yoneda, K., Banchereau, J., Caux, C. et al. 1999. The
430 monoclonal antibody DCGM4 recognizes Langerin, a protein specific of Langerhans
431 cells, and is rapidly internalized from the cell surface. *Eur. J. Immunol.* **29**, 2695-2704.

432 Geijtenbeek, T.B., Kwon, D.S., Torensma, R., van, Vliet S.J., van, Duijnhoven G.C.,
433 Middel, J., Cornelissen, I.L., Nottet, H.S., KewalRamani, V.N., Littman, D.R. et al. 2000.
434 DC-SIGN, a dendritic cell-specific HIV-1-binding protein that enhances trans-infection of
435 T cells. *Cell.* **100**, 587-597.
436 Geijtenbeek, T.B., Krooshoop, D.J., Bleijs, D.A., van, Vliet S.J., van, Duijnhoven G.C.,
437 Grabovsky, V., Alon, R., Figdor, C.G., and van, Kooyk Y. 2000. DC-SIGN-ICAM-2
438 interaction mediates dendritic cell trafficking. *Nat. Immunol.* **1**, 353-357.
439 Kawamura, T., Cohen, S.S., Borris, D.L., Aquilino, E.A., Glushakova, S., Margolis, L.B.,
440 Orenstein, J.M., Offord, R.E., Neurath, A.R., and Blauvelt, A. 2000. Candidate
441 microbicides block HIV-1 infection of human immature Langerhans cells within
442 epithelial tissue explants. *J. Exp. Med.* **192**, 1491-1500.
443 Salmon, P., Oberholzer, J., Occhiodoro, T., Morel, P., Lou, J., and Trono, D. 2000.
444 Reversible immortalization of human primary cells by lentivector-mediated transfer of
445 specific genes. *Mol. Ther.* **2**, 404-414.
446 Valladeau, J., Ravel, O., Dezutter-Dambuyant, C., Moore, K., Kleijmeer, M., Liu, Y.,
447 Duvert-Frances, V., Vincent, C., Schmitt, D., Davoust, J. et al. 2000. Langerin, a novel C-
448 type lectin specific to Langerhans cells, is an endocytic receptor that induces the formation
449 of Birbeck granules. *Immunity.* **12**, 71-81.
450 Kawamura, T., Qualbani, M., Thomas, E.K., Orenstein, J.M., and Blauvelt, A. 2001. Low
451 levels of productive HIV infection in Langerhans cell-like dendritic cells differentiated in
452 the presence of TGF-beta1 and increased viral replication with CD40 ligand-induced
453 maturation. *Eur. J. Immunol.* **31**, 360-368.

454 Figdor, C.G., van, Kooyk Y., and Adema, G.J. 2002. C-type lectin receptors on dendritic
455 cells and Langerhans cells. *Nat. Rev. Immunol.* **2**, 77-84.
456 Mc, Dermott R., Ziylan, U., Spehner, D., Bausinger, H., Lipsker, D., Mommaas, M.,
457 Cazenave, J.P., Raposo, G., Goud, B., de, la Salle H. et al. 2002. Birbeck granules are
458 subdomains of endosomal recycling compartment in human epidermal Langerhans cells,
459 which form where Langerin accumulates. *Mol. Biol. Cell.* **13**, 317-335.
460 Turville, S.G., Cameron, P.U., Handley, A., Lin, G., Pohlmann, S., Doms, R.W., and
461 Cunningham, A.L. 2002. Diversity of receptors binding HIV on dendritic cell subsets. *Nat.*
462 *Immunol.* **3**, 975-983.
463 Stambach, N.S., and Taylor, M.E. 2003. Characterization of carbohydrate recognition by
464 langerin, a C-type lectin of Langerhans cells. *Glycobiology.* **13**, 401-410.
465 Stewart, S.A., Dykxhoorn, D.M., Palliser, D., Mizuno, H., Yu, E.Y., An, D.S., Sabatini,
466 D.M., Chen, I.S., Hahn, W.C., Sharp, P.A. et al. 2003. Lentivirus-delivered stable gene
467 silencing by RNAi in primary cells. *RNA.* **9**, 493-501.
468 Valladeau, J., Dezutter-Dambuyant, C., and Saeland, S. 2003. Langerin/CD207 sheds light
469 on formation of birbeck granules and their possible function in Langerhans cells.
470 *Immunol. Res.* **28**, 93-107.
471 Guo, Y., Feinberg, H., Conroy, E., Mitchell, D.A., Alvarez, R., Blixt, O., Taylor, M.E.,
472 Weis, W.I., and Drickamer, K. 2004. Structural basis for distinct ligand-binding and
473 targeting properties of the receptors DC-SIGN and DC-SIGNR. *Nat. Struct. Mol. Biol.*
474 **11**, 591-598.
475 Hunger, R.E., Sieling, P.A., Ochoa, M.T., Sugaya, M., Burdick, A.E., Rea, T.H., Brennan,

476 P.J., Belisle, J.T., Blauvelt, A., Porcelli, S.A. et al. 2004. Langerhans cells utilize CD1a and
477 langerin to efficiently present nonpeptide antigens to T cells. *J. Clin. Invest.* **113**, 701-
478 708.
479 McDermott, R., Bausinger, H., Fricker, D., Spehner, D., Proamer, F., Lipsker, D.,
480 Cazenave, J.P., Goud, B., De, La Salle H., Salamero, J. et al. 2004. Reproduction of
481 Langerin/CD207 traffic and Birbeck granule formation in a human cell line model. *J.*
482 *Invest. Dermatol.* **123**, 72-77.
483 Pettersen, E.F., Goddard, T.D., Huang, C.C., Couch, G.S., Greenblatt, D.M., Meng, E.C.,
484 and Ferrin, T.E. 2004. UCSF Chimera--a visualization system for exploratory research and
485 analysis. *J. Comput. Chem.* **25**, 1605-1612.
486 Takahara, K., Yashima, Y., Omatsu, Y., Yoshida, H., Kimura, Y., Kang, Y.S., Steinman,
487 R.M., Park, C.G., and Inaba, K. 2004. Functional comparison of the mouse DC-SIGN,
488 SIGNR1, SIGNR3 and Langerin, C-type lectins. *Int. Immunol.* **16**, 819-829.
489 Mastronarde, D.N. 2005. Automated electron microscope tomography using robust
490 prediction of specimen movements. *J. Struct. Biol.* **152**, 36-51.
491 Verdijk, P., Dijkman, R., Plasmeijer, E.I., Mulder, A.A., Zoutman, W.H., Mieke,
492 Mommaas A., and Tensen, C.P. 2005. A lack of Birbeck granules in Langerhans cells is
493 associated with a naturally occurring point mutation in the human Langerin gene. *J.*
494 *Invest. Dermatol.* **124**, 714-717.
495 Nicastro, D., Schwartz, C., Pierson, J., Gaudette, R., Porter, M.E., and McIntosh, J.R. 2006.
496 The molecular architecture of axonemes revealed by cryoelectron tomography. *Science.*
497 **313**, 944-948.

498 Pokidysheva, E., Zhang, Y., Battisti, A.J., Bator-Kelly, C.M., Chipman, P.R., Xiao, C.,
499 Gregorio, G.G., Hendrickson, W.A., Kuhn, R.J., and Rossmann, M.G. 2006. Cryo-EM
500 reconstruction of dengue virus in complex with the carbohydrate recognition domain of
501 DC-SIGN. *Cell.* **124**, 485-493.
502 de_Witte, L., Nabatov, A., Pion, M., Fluitsma, D., de, Jong M.A., de, Gruijl T., Piguet, V.,
503 van, Kooyk Y., and Geijtenbeek, T.B. 2007. Langerin is a natural barrier to HIV-1
504 transmission by Langerhans cells. *Nat. Med.* **13**, 367-371.
505 Metlagel, Z., Kikkawa, Y.S., and Kikkawa, M. 2007. Ruby-Helix: an implementation of
506 helical image processing based on object-oriented scripting language. *J. Struct. Biol.* **157**,
507 95-105.
508 Chatwell, L., Holla, A., Kaufer, B.B., and Skerra, A. 2008. The carbohydrate recognition
509 domain of Langerin reveals high structural similarity with the one of DC-SIGN but an
510 additional, calcium-independent sugar-binding site. *Mol. Immunol.* **45**, 1981-1994.
511 Merad, M., Ginhoux, F., and Collin, M. 2008. Origin, homeostasis and function of
512 Langerhans cells and other langerin-expressing dendritic cells. *Nat. Rev. Immunol.* **8**, 935-
513 947.
514 Schaefer, M.R., Williams, M., Kulpa, D.A., Blakely, P.K., Yaffee, A.Q., and Collins, K.L.
515 2008. A novel trafficking signal within the HLA-C cytoplasmic tail allows regulated
516 expression upon differentiation of macrophages. *J. Immunol.* **180**, 7804-7817.
517 Cambi, A., Beeren, I., Joosten, B., Fransen, J.A., and Figdor, C.G. 2009. The C-type lectin
518 DC-SIGN internalizes soluble antigens and HIV-1 virions via a clathrin-dependent
519 mechanism. *Eur. J. Immunol.* **39**, 1923-1928.

520 Thepaut, M., Valladeau, J., Nurisso, A., Kahn, R., Arnou, B., Vives, C., Saeland, S., Ebel,
521 C., Monnier, C., Dezutter-Dambuyant, C. et al. 2009. Structural studies of langerin and
522 Birbeck granule: a macromolecular organization model. *Biochemistry.* **48**, 2684-2698.
523 Adams, P.D., Afonine, P.V., Bunkoczi, G., Chen, V.B., Davis, I.W., Echols, N., Headd,
524 J.J., Hung, L.W., Kapral, G.J., Grosse-Kunstleve, R.W. et al. 2010. PHENIX: a
525 comprehensive Python-based system for macromolecular structure solution. *Acta.*
526 *Crystallogr. D. Biol. Crystallogr.* **66**, 213-221.
527 de_Jong, M.A., de, Witte L., Taylor, M.E., and Geijtenbeek, T.B. 2010. Herpes simplex
528 virus type 2 enhances HIV-1 susceptibility by affecting Langerhans cell function. *J.*
529 *Immunol.* **185**, 1633-1641.
530 de_Jong MA, Geijtenbeek T.B. 2010. Langerhans cells in innate defense against pathogens.
531 *Trends. Immunol.* **31**, 452-459.
532 Feinberg, H., Powlesland, A.S., Taylor, M.E., and Weis, W.I. 2010. Trimeric structure of
533 langerin. *J. Biol. Chem.* **285**, 13285-13293.
534 Tateno, H., Ohnishi, K., Yabe, R., Hayatsu, N., Sato, T., Takeya, M., Narimatsu, H., and
535 Hirabayashi, J. 2010. Dual specificity of Langerin to sulfated and mannosylated glycans via
536 a single C-type carbohydrate recognition domain. *J. Biol. Chem.* **285**, 6390-6400.
537 Schindelin, J., Arganda-Carreras, I., Frise, E., Kaynig, V., Longair, M., Pietzsch, T.,
538 Preibisch, S., Rueden, C., Saalfeld, S., Schmid, B. et al. 2012. Fiji: an open-source platform
539 for biological-image analysis. *Nat. Methods.* **9**, 676-682.
540 Schneider, C.A., Rasband, W.S., and Eliceiri, K.W. 2012. NIH Image to ImageJ: 25 years
541 of image analysis. *Nat. Methods.* **9**, 671-675.

542 Cole, N.B. 2013. Site-specific protein labeling with SNAP-tags. *Curr. Protoc. Protein. Sci.*
543 **73**, 30.1.1-30.1.16.
544 Lenormand, C., Spiegelhalter, C., Cinquin, B., Bardin, S., Bausinger, H., Angenieux, C.,
545 Eckly, A., Proamer, F., Wall, D., Lich, B. et al. 2013. Birbeck granule-like "organized
546 smooth endoplasmic reticulum" resulting from the expression of a cytoplasmic YFP-tagged
547 langerin. *PLoS. One.* **8**, e60813.
548 Ogawa, Y., Kawamura, T., Matsuzawa, T., Aoki, R., Gee, P., Yamashita, A., Moriishi, K.,
549 Yamasaki, K., Koyanagi, Y., Blauvelt, A. et al. 2013. Antimicrobial peptide LL-37
550 produced by HSV-2-infected keratinocytes enhances HIV infection of Langerhans cells.
551 *Cell. Host. Microbe.* **13**, 77-86.
552 Burkard, C., Bloyet, L.M., Wicht, O., van, Kuppeveld F.J., Rottier, P.J., de, Haan C.A., and
553 Bosch, B.J. 2014. Dissecting virus entry: replication-independent analysis of virus binding,
554 internalization, and penetration using minimal complementation of beta-galactosidase.
555 *PLoS. One.* **9**, e101762.
556 Oda, T., Yanagisawa, H., and Kikkawa, M. 2015. Detailed structural and biochemical
557 characterization of the nexin-dynein regulatory complex. *Mol. Biol. Cell.* **26**, 294-304.
558 Ribeiro, C.M., Sarrami-Forooshani, R., Setiawan, L.C., Zijlstra-Willems, E.M., van,
559 Hamme J.L., Tigchelaar, W., van, der Wel N.N., Kootstra, N.A., Gringhuis, S.I., and
560 Geijtenbeek, T.B. 2016. Receptor usage dictates HIV-1 restriction by human TRIM5alpha
561 in dendritic cell subsets. *Nature.* **540**, 448-452.
562 Stewart-Jones, G.B., Soto, C., Lemmin, T., Chuang, G.Y., Druz, A., Kong, R., Thomas,
563 P.V., Wagh, K., Zhou, T., Behrens, A.J. et al. 2016. Trimeric HIV-1-Env Structures Define

564 Glycan Shields from Clades A, B, and G. *Cell.* **165**, 813-826.

565 Doebel, T., Voisin, B., and Nagao, K. 2017. Langerhans Cells - The Macrophage in
566 Dendritic Cell Clothing. *Trends. Immunol.* **38**, 817-828.

567 Zheng, S.Q., Palovcak, E., Armache, J.P., Verba, K.A., Cheng, Y., and Agard, D.A. 2017.
568 MotionCor2: anisotropic correction of beam-induced motion for improved cryo-electron
569 microscopy. *Nat. Methods.* **14**, 331-332.

570 Goddard, T.D., Huang, C.C., Meng, E.C., Pettersen, E.F., Couch, G.S., Morris, J.H., and
571 Ferrin, T.E. 2018. UCSF ChimeraX: Meeting modern challenges in visualization and
572 analysis. *Protein. Sci.* **27**, 14-25.

573 Nakane, T., Kimanius, D., Lindahl, E., and Scheres, S.H. 2018. Characterisation of
574 molecular motions in cryo-EM single-particle data by multi-body refinement in RELION.
575 *Elife.* **7**, e36861.

576 Gonelli, C.A., Khoury, G., Center, R.J., and Purcell, D.F.J. 2019. HIV-1-based Virus-like
577 Particles that Morphologically Resemble Mature, Infectious HIV-1 Virions. *Viruses.* **11**,
578 507.

579 Heredia, J.D., Park, J., Choi, H., Gill, K.S., and Procko, E. 2019. Conformational
580 Engineering of HIV-1 Env Based on Mutational Tolerance in the CD4 and PG16 Bound
581 States. *J. Virol.* **93**, e00219-00219.

582 Postma, M., and Goedhart, J. 2019. PlotsOfData-A web app for visualizing data together
583 with their summaries. *PLoS. Biol.* **17**, e3000202.

584 Pan, J., Peng, H., Chen, B., and Harrison, S.C. 2020. Cryo-EM Structure of Full-length
585 HIV-1 Env Bound With the Fab of Antibody PG16. *J. Mol. Biol.* **432**, 1158-1168.

586 Thornton, S.M., Samararatne, V.D., Skeate, J.G., Buser, C., Luhen, K.P., Taylor, J.R., Da,
587 Silva D.M., and Kast, W.M. 2020. The Essential Role of anxA2 in Langerhans Cell
588 Birbeck Granules Formation. *Cells.* **9**, 974.
589 Valverde, P., Martテュnez, J.D., Caテアada, F.J., Ardテ。, A., and Jimテゥnez-Barbero, J. 2020.
590 Molecular Recognition in C-Type Lectins: The Cases of DC-SIGN, Langerin, MGL, and
591 L-Sectin. *Chembiochem.* **21**, 2999-3025.
592 Kimanius, D., Dong, L., Sharov, G., Nakane, T., and Scheres, S.H.W. 2021. New tools for
593 automated cryo-EM single-particle analysis in RELION-4.0. *Biochem. J.* **478**, 4169-4185.
594 Rhodes, J.W., Botting, R.A., Bertram, K.M., Vine, E.E., Rana, H., Baharlou, H., Vegh, P.,
595 O'Neil, T.R., Ashhurst, A.S., Fletcher, J. et al. 2021. Human anogenital monocyte-derived
596 dendritic cells and langerin+cDC2 are major HIV target cells. *Nat. Commun.* **12**, 2147.
597
598

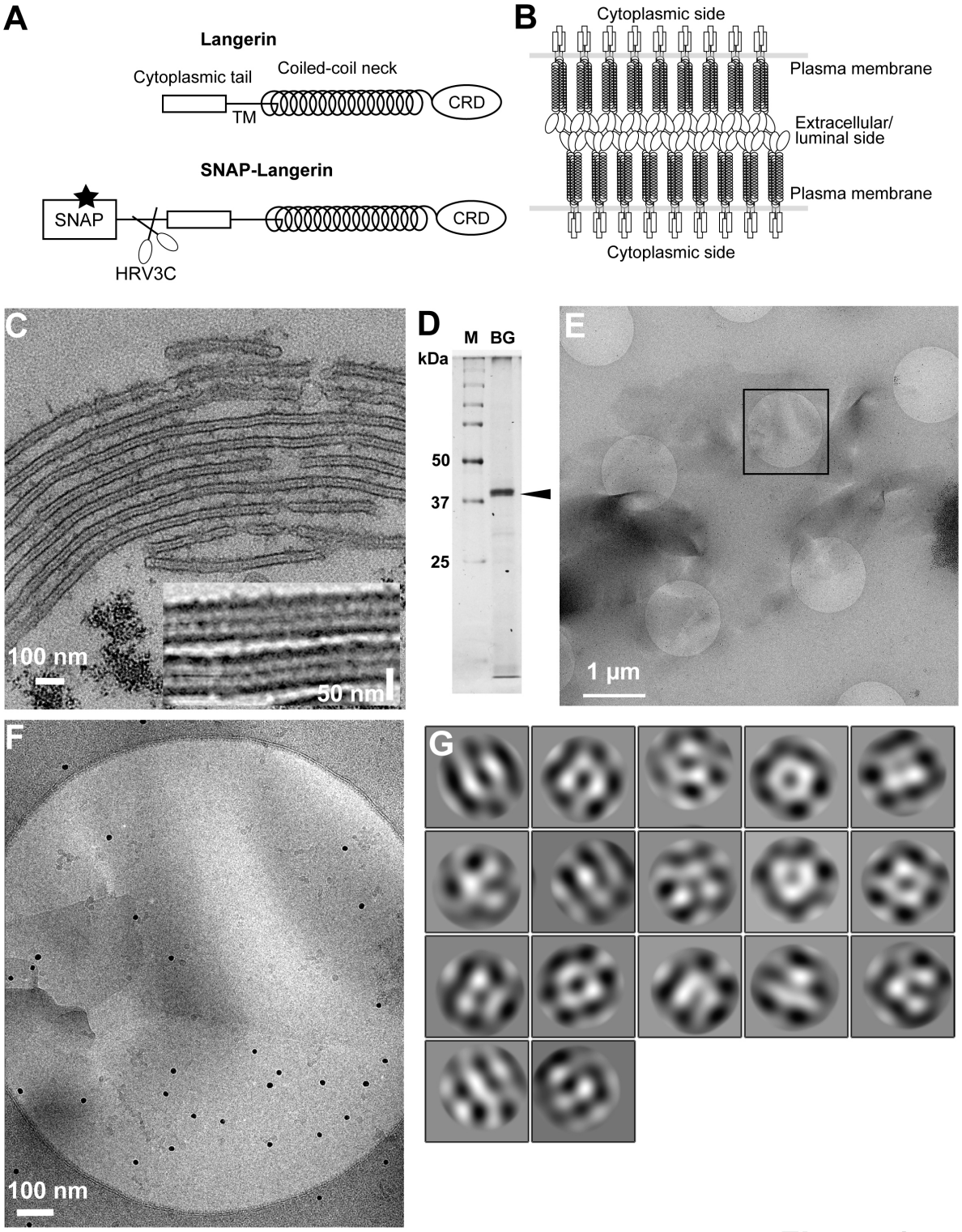
A
Langerin
Cytoplasmic tail
Coiled-coil neck
TM
CRD
SNAP-Langerin
SNAP
CRD
HRV3C
B
Cytoplasmic side
Plasma membrane
Extracellular/
luminal side
Plasma membrane
Cytoplasmic side
C
100 nm
50 nm
D
M
BG
kDa
50
37
25
E
1 µm
F
100 nm
G

Figure 1

599

600 **Figure 1: Isolation of Birbeck granules.** (A) Domain organization of langerin. Human
601 langerin is a 328-amino acids protein composed of an N-terminal cytoplasmic tail, a
602 transmembrane domain (TM), a coiled-coil neck, and a C-terminal carbohydrate-recognition
603 domain (CRD). We fused a SNAP-tag at the N-terminus of langerin and inserted an HRV3C
604 protease cleavage site between the tag and the langerin sequences. For streptavidin-mediated
605 precipitation of Birbeck granules, the SNAP-tag was biotinylated (star). (B) Model of
606 langerin oligomerization within Birbeck granules. Langerin trimers bind to each other face-
607 to-face via the CRDs, bringing the two layers of the plasma membrane closer together. (C)
608 Birbeck granules formed in 293T cells overexpressing langerin. Addition of yeast mannan
609 induced the formation of Birbeck granules a few micrometers long. Inset shows a magnified
610 view of Birbeck granules. (D) SDS-PAGE of isolated Birbeck granules. Purified langerin
611 (arrowhead) was released from streptavidin-agarose by HRV3C digestion. M: molecular
612 weight marker; and BG: isolated Birbeck granules. (E) Cryo-electron microscopy of isolated
613 Birbeck granules. Black square indicates the position of the close-up view shown in F. (F)
614 Wavy lamellar structure of the Birbeck granule. Black dots were gold nanoparticles used as
615 fiducial markers. (G) Class averages of the projection images of Birbeck granules. The image
616 dimension is 34 nm^2. Although 2D classification did not converge well due to the continuity

of the structure, some classes showed a porous structure with a honeycomb-like lattice.

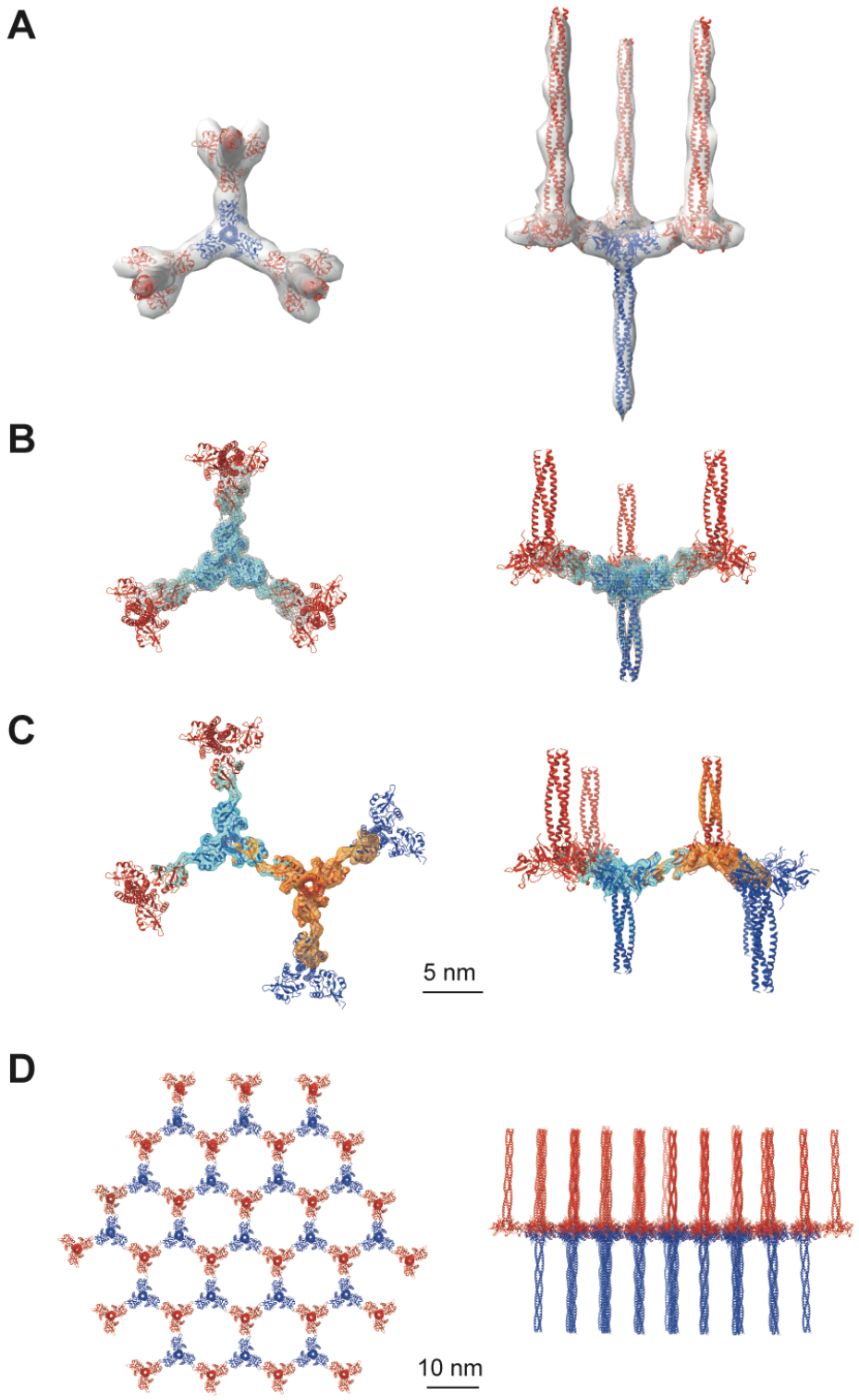

Figure 2

620

621 **Figure 2: Averaged subtomograms of Birbeck granules. (**A) Result of the initial 3D
622 refinement. The central langerin trimer (blue) binds to the three inverted langerin trimers
623 (red). (B) Result of the focused refinement. Improved resolution (6.4 Å) allowed secondary
624 structure modeling. The gray mesh and the cyan surface indicate low and high threshold
625 isosurfaces, respectively. (C) Result of the two-body refinement. The second body (orange)
626 was refined with respect to the first body (cyan). (D) Honeycomb model of the langerin lattice
627 within Birbeck granules. This honeycomb lattice is an ideal model, with the assumption of
628 structural uniformity. (A-D) left, top views; right, side views.
629
630

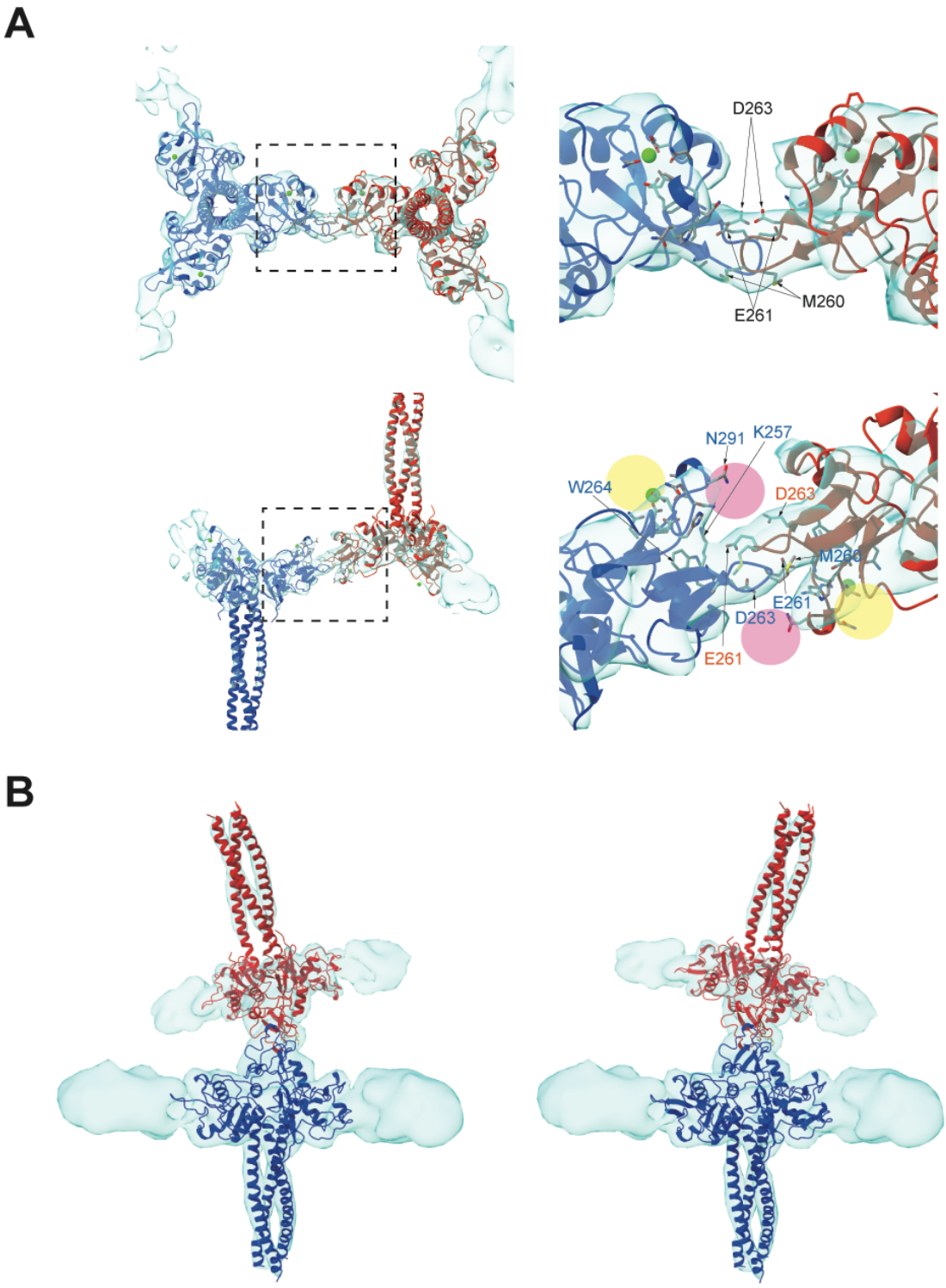

Figure 3

631

632 **Figure 3: Binding interface between two langerin trimers.** (A) Two langerin trimers
633 interact via the loops at residues 258-263. Amino acid codes and residue numbers are
634 indicated. Yellow and pink circles indicate the primary and secondary carbohydrate-binding
635 sites. The orientations of the side chains are speculative because the resolution of these maps
636 (6.4 Å) was insufficient for precise modeling. Calcium ions (green) were placed based on the
637 crystal structure (PDB ID: 3KQG). Top and side views are displayed in the top and bottom
638 rows, respectively. Broken squares indicate the positions of the magnified views on the right.
639 (B) Flexibility between the two trimers. The first eigenvector of the structural variation of
640 the inverted trimer (red) relative to the upright trimer (blue) shows an approximately 30°
641 rotation about the loop 258-263 (see Movie S2).
642
643

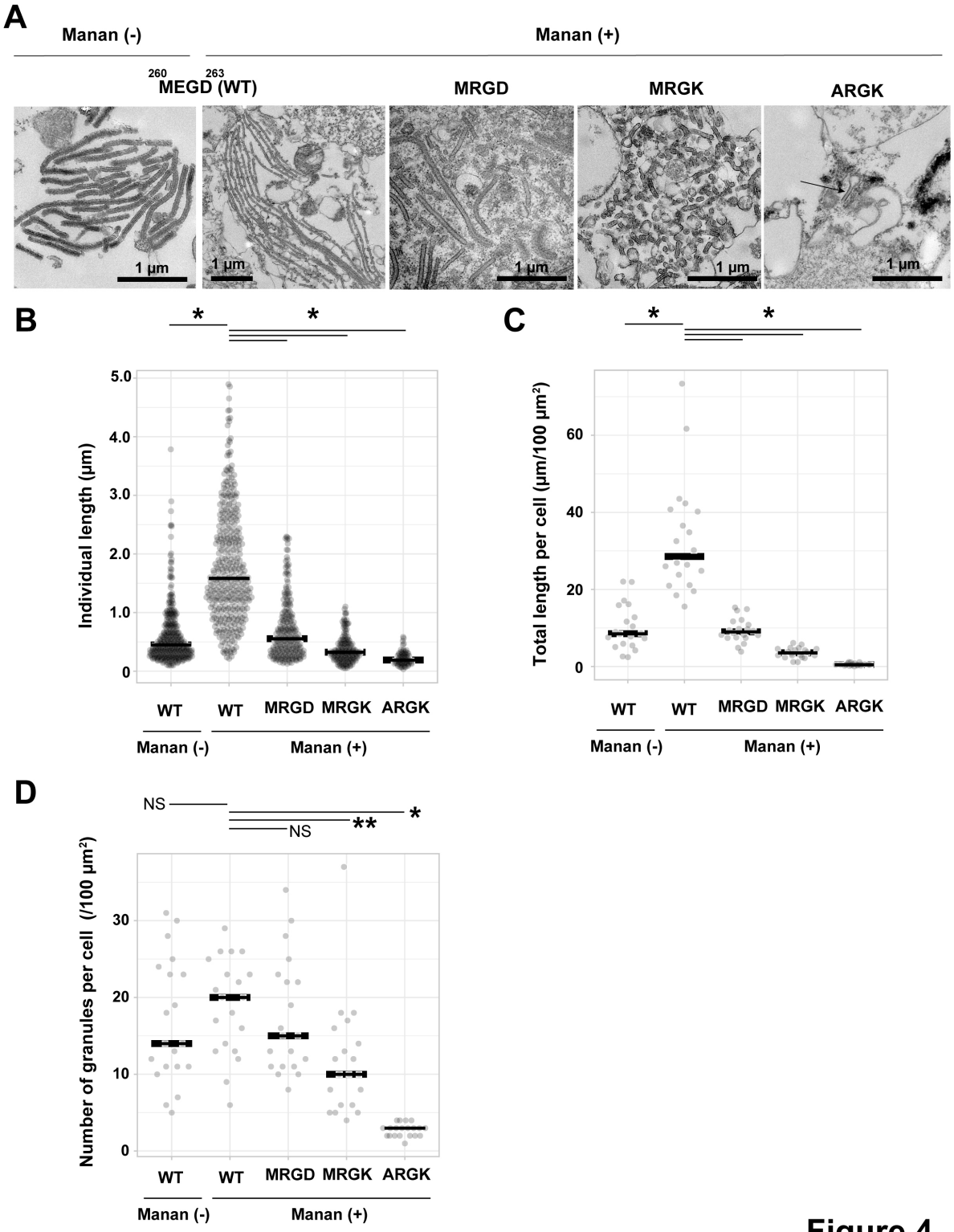
A
Manan (-)
Manan (+)
260 263
MEGD (WT)
MRGD
MRGK
ARGK
1 µm
B
Individual length (µm)
5.0
4.0
3.0
2.0
1.0
0
WT
WT
MRGD
MRGK
ARGK
Manan (-)
Manan (+)
C
Total length per cell (µm/100 µm²)
60
40
20
0
D
NS
NS
**
*
Number of granules per cell (/100 µm²)
30
20
10
0

Figure 4

645 **Figure 4: Mutations to the loop 258-263 disrupted Birbeck granule formation.** (A) Ultra-
646 thin electron microscopy of Birbeck granules with and without yeast mannan in langerin-
647 overexpressing 293T cells. Residues at 260-263 (Met-Glu-Gly-Asp, MEGD) were mutated
648 to Met-Arg-Gly-Asp (MRGD), Met-Arg-Gly-Lys (MRGK), or Ala-Arg-Gly-Lys (ARGK).
649 The Mannan (+) WT image has a lower magnification than the others in order to show the
650 entire Birbeck granules. (B-D) Quantification of Birbeck granule formation. Horizontal lines
651 indicate the median values. Single asterisks and the double asterisk indicate statistically
652 significant differences with $p < 0.01$ and $p = 0.0101$, respectively. NS indicates no statistically
653 significant differences. *p* values were calculated using Bonferroni-corrected Student's *t*-tests.
654 (B) Lengths of individual Birbeck granules were measured. N = 337 (WT mannan-), 386
655 (WT mannan+), 348 (MRGD), 233 (MRGK), and 70 (ARGK). (C) Sum of the length of
656 Birbeck granules per 100 μm^2 cell area. Cross-sections of cells with nuclei of > 5 μm in
657 diameter were selected and the total lengths of the Birbeck granules were measured within
658 the cells. N = 20 for all the samples. (D) Number of the Birbeck granules per 100 μm^2 cell
659 area. N = 20 for all the samples.
660
661

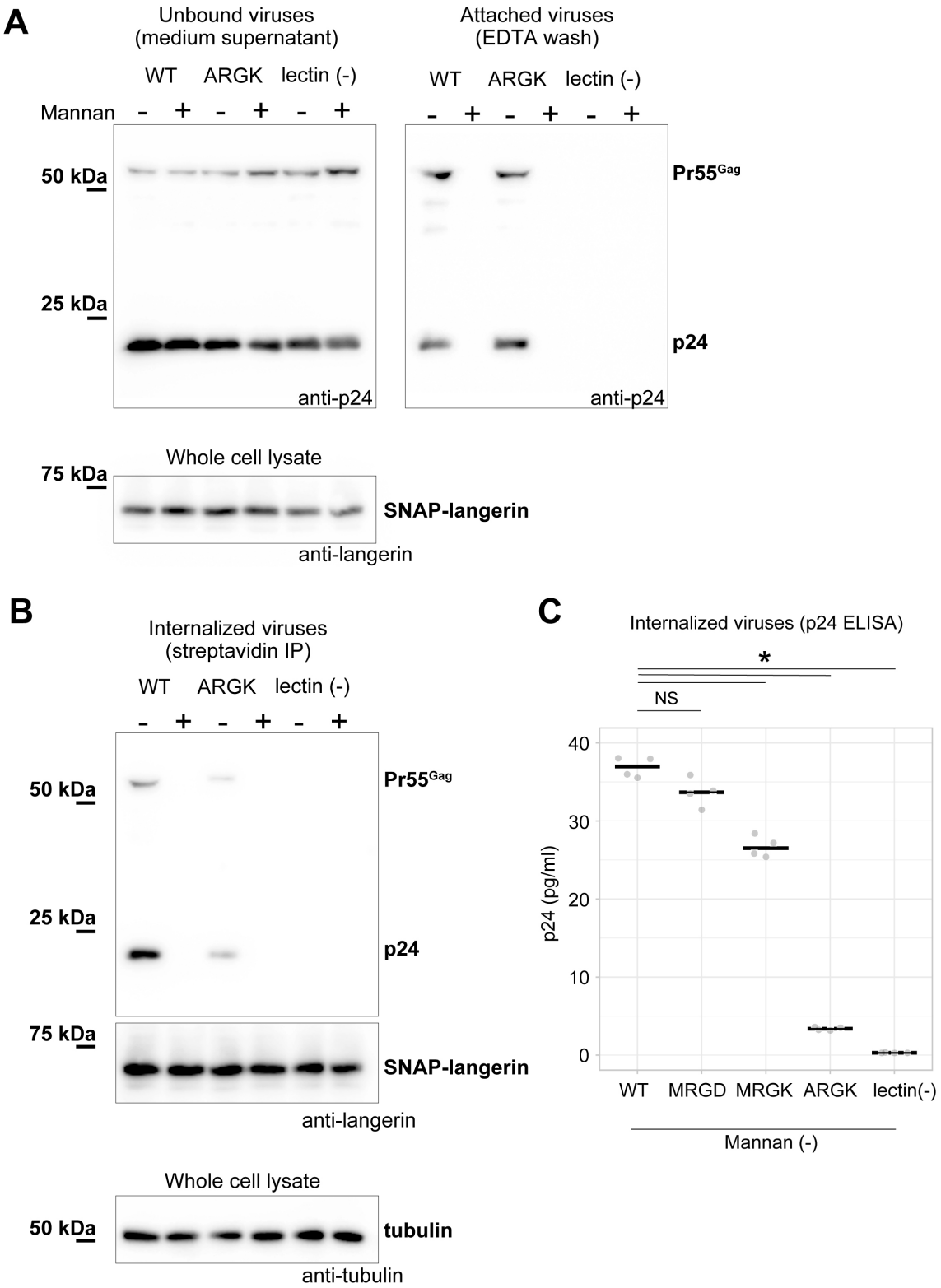
A
Unbound viruses
(medium supernatant)
Attached viruses
(EDTA wash)
WT ARGK lectin (-)
WT ARGK lectin (-)
Mannan - + - + - +
- + - + - +
50 kDa
25 kDa
Pr55Gag
p24
anti-p24
anti-p24
Whole cell lysate
75 kDa
SNAP-langerin
anti-langerin
B
Internalized viruses
(streptavidin IP)
WT ARGK lectin (-)
- + - + - +
50 kDa
25 kDa
75 kDa
Pr55Gag
p24
SNAP-langerin
anti-langerin
Whole cell lysate
50 kDa
tubulin
anti-tubulin
C
Internalized viruses (p24 ELISA)
*
NS
p24 (pg/ml)
40
30
20
10
0
WT MRGD MRGK ARGK lectin(-)
Mannan (-)

Figure 5

662

663 **Figure 5: Mutation to the loop 258-263 inhibited the internalization of pseudoviruses.**
664 HIV-1 pseudoviruses were added to langerin-expressing 293T cells. Yeast mannan (10
665 μg/ml) was added to block the lectin-dependent binding of pseudoviruses. A langerin mutant
666 lacking calcium binding ability (lectin (-)) was used as the negative control. (A) Immunoblots
667 of pseudoviruses attached to the cell surface. Unbound and attached viruses were collected
668 from the supernatant of the culture medium and TBS-EDTA buffer, respectively. Samples of
669 unbound viruses were diluted 50-fold to adjust the band intensities. The expression levels of
670 SNAP-tagged langerin show that the numbers of transfected cells were approximately the
671 same in each experiment. $Pr55^{gag}$ and p24 indicate unprocessed and fully-processed capsid
672 proteins, respectively. (B) Immunoblots of internalized pseudoviruses. Birbeck granules were
673 isolated by precipitation using streptavidin-agarose, and intracellular viruses and langerin
674 were detected by their respective antibodies. Tubulins in the whole-cell lysates were detected
675 for loading controls. (C) Quantification of internalized viruses using p24 ELISA. Horizontal
676 lines indicate the mean. NS and Asterisk indicate no significant difference and statistically
677 significant differences ($p < 0.001$) calculated using Bonferroni-corrected Student's *t*-tests
678 (N=4), respectively.
679

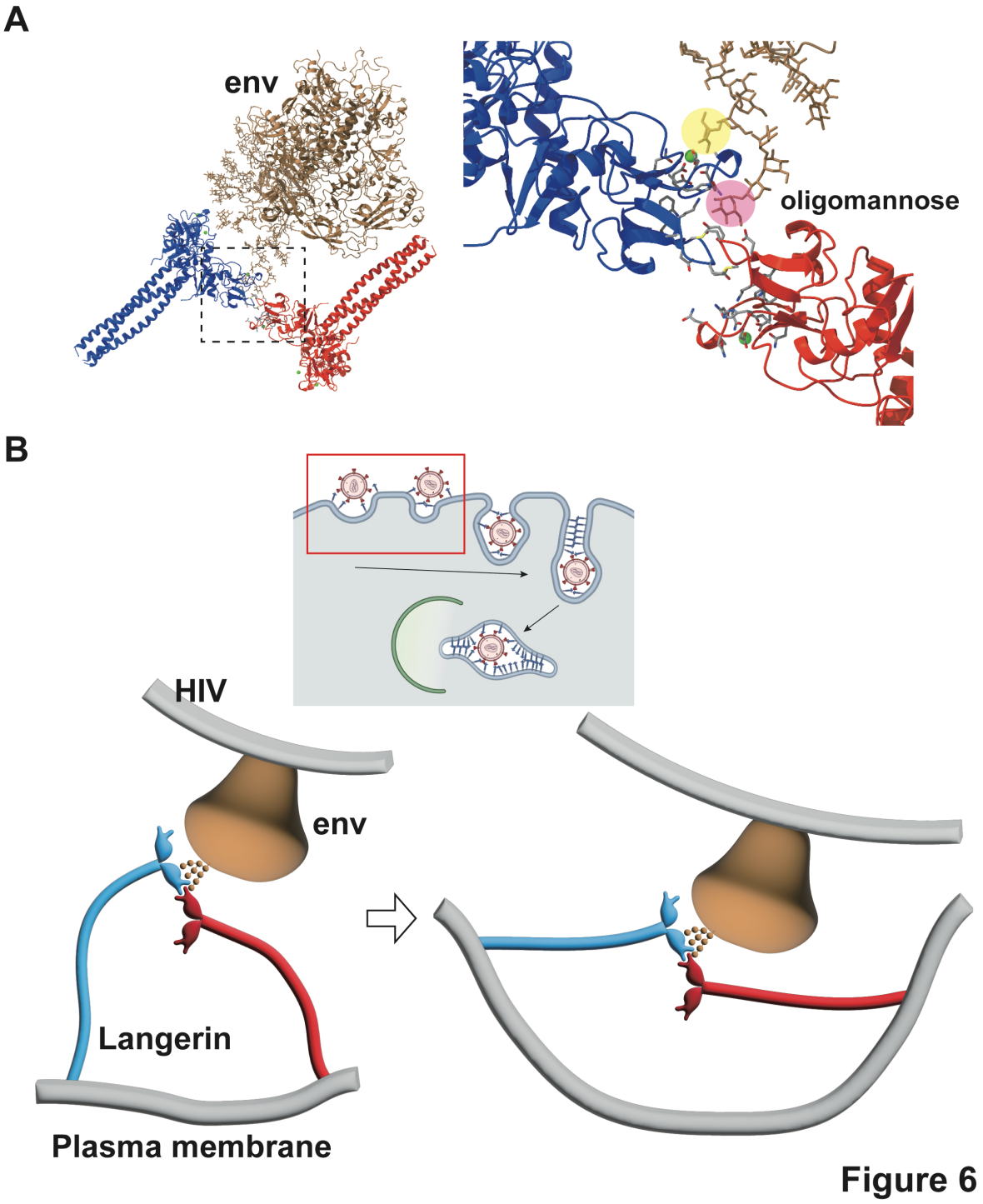

680

681 **Figure 6: Model of HIV internalization by langerin.** (A) Glycosylated structure of HIV-1

envelope (env, gray) (Constructed based on PDB ID: 5FYJ and 6ULC) bound to the langerin trimer complex. Branches of the high-mannose oligosaccharide interacting with the primary (yellow) and secondary (pink) carbohydrate-binding sites. The broken square indicates the position of the close-up view on the right. (B) Schematics of HIV internalization by langerin. The inset on the top shows an overview of antigen processing within a Langerhans cell. Viruses are captured by langerin, internalized into a Birbeck granule, and degraded by the autophagic system. The red square indicates the viral entry process described in the lower panels. The high-mannose oligosaccharide on HIV-1 env first binds to the primary carbohydrate-binding site, and one of the branches of the oligo-mannose weakly interacts with the secondary binding site. The flexible neck region allows docking of the loop 258-263 of an adjacent trimer into the secondary carbohydrate-binding cleft, reinforcing the binding of the oligo-mannose. As the elastic neck regions straighten, the plasma membrane is deformed into a lamellar invagination, which internalizes the virus.

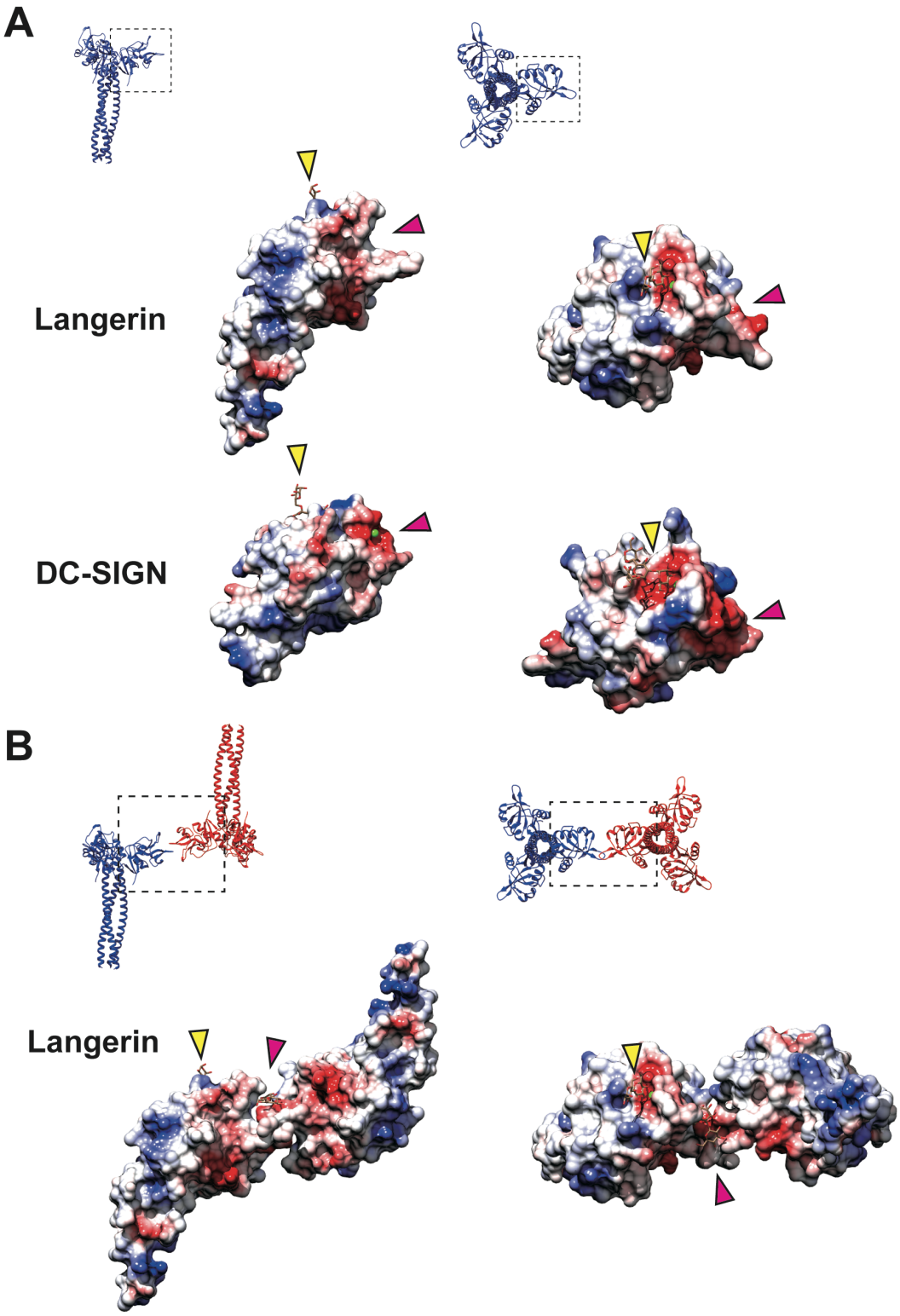

Figure 7

697

698 **Figure 7: Coulombic surfaces of the carbohydrate-binding sites.** (A) Comparison of the
699 surface charge between the CRDs of langerin and DC-SIGN (PDB ID: 1SL4). Blue and red
700 coloring indicates positive and negative charges, respectively. The primary and secondary
701 carbohydrate-binding sites are indicated by yellow and pink arrowheads, respectively. The
702 region of DC-SIGN corresponding to the secondary carbohydrate-binding sites of langerin is
703 occupied by calcium ions (green) and does not form a cleft. (B) Surface model of the langerin
704 trimer complex. Mannose ligands are placed based on a previously proposed model (Chatwell
705 et al., 2008). (A-B) Broken squares indicate the position and the orientation of the side (left)
706 and the top (right) views. Oligosaccharide ligands are shown in gray.
707
708